Plasma preheating technology for replicating planetary re-entry surface temperatures

D.O. Iyinomen

Mechanical and Aerospace Engineering, Aerospace Research and Innovations
E-mail: iyidaniel@yahoo.co.uk

Abstract

Arc-jet facilities have been the norm for ablation experiments used to calibrate computational models to date. However, the arc jet has a few major limitations and challenges, including non-uniform enthalpy distribution, non-equilibrium state, change of surface quality during testing and the extent of oxidation, to name but a few. A novel plasma technique for preheating axisymmetric heatshield samples in hypersonic impulse facilities is presented herein. The major aim of this innovative work is to help reduce the large variations of ablation rate predictions, space vehicle materials and missile design/testing, obtain strongly coupled hypersonic boundary layers and achieve lower cost of aerothermodynamics experiments. This present work remains one of the most highly anticipated solutions to maximise payload success and replicate high surface temperatures identical to those experienced by real flight vehicles. This work makes a useful contribution to re-entry studies under conditions that replicate the characteristics of re-entry flights. Future applications for the technique are expected to be found in hypersonic impulse facilities that can simulate the true flow energy under re-entry conditions.

NOMENCLATURE

|	
I	Current
V	Applied voltage
R	Resistance
k	Thermal conductivity of material
dT/dr	Temperature gradient in the radial direction
A	Area of heat application
h	Convective heat transfer coefficient
T	Surface temperature
T_∞	Ambient temperature
ρ	Density
c_p	Specific heat capacity
ε	Emissivity
σ	Stefan-Boltzmann Constant
dr	Arbitrary radius
A_{cs}	Cross-sectional area
μ	Resistivity
$q(r)$	Net flux
Q_{max}	Maximum heat intensity
Q_{Net}	Net heat flux
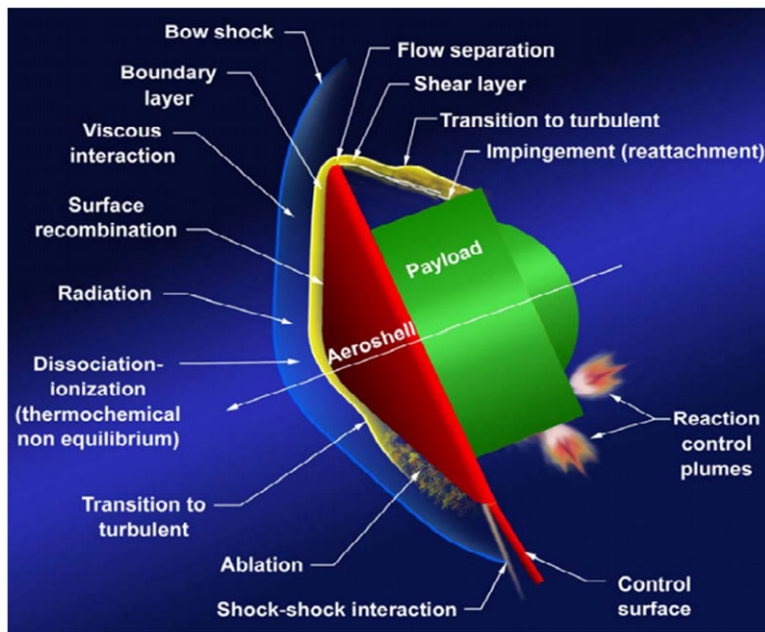
Figure 1. *Flow phenomena during re-entry, descent and landing [15].*

1.0 INTRODUCTION

The National Aeronautics and Space Administration (NASA) planetary program continues to fly blunt bodies as entry probes [1], and computational models of the heat loads experienced during atmospheric re-entries [2,3] are continually being updated [4]. Validation of these models is critical for the safe and economic design of future flight vehicles [5,6]. A planetary entry vehicle must reduce the entry velocity sufficiently to complete its mission successfully, as these vehicles are required to be high-drag devices [7]. As the vehicle starts to descend from the highest altitudes (free molecular regime) through the transitional regime to the continuum regime, the gas becomes denser while the aerodynamics forces and heating rates increase rapidly [8]. At near- or super-orbital velocities ($V_\infty \geq 11$km/s), a strong bow shock envelopes the vehicle and the total energy per unit mass of atmospheric gas crossing the bow shock ($\frac{1}{2}V_\infty^2$) becomes sufficiently large to cause significant dissociation and ionisation reactions behind the shock [9]. Proper analysis of the heat flux [10], gas–surface interactions [11] and properties of heatshield materials [12] are needed for ablation performance evaluations [13,14]. Thermochemical processes of blunt bodies during re-entry, descent and landing, in addition to the corresponding base flow phenomenon, are illustrated schematically in Fig. 1. The most common geometries employed for entry into planetary atmospheres are blunt body configurations such as those of the Mercury, Gemini, Apollo, Orion, Viking, Huygens, Pioneer, FIRE II, ARD and OREX vehicles as well as all Sample Return Capsules (SRC) such as Genesis-SRC, Hayabusa-SRC and Stardust-SRC [16–18].

The primary features of a hypersonic and high-enthalpy flow are high kinetic energy and high stagnation temperature [19]. In high-enthalpy facilities, the gas is either partially or totally dissociated before reaching the surface. Using such facilities for Martian re-entry studies, carbon dioxide molecules do not get to the surface because they start to dissociate inside the arc chamber, having some consequences for the nozzle flow. This has some significant effects on the validity of experimental data. In addition, the use of a gas different from air, such as a CO_2 environment, has a strong impact on the arc chamber and notably on the arc performance in most high-enthalpy facilities such as the ONERA wind tunnels
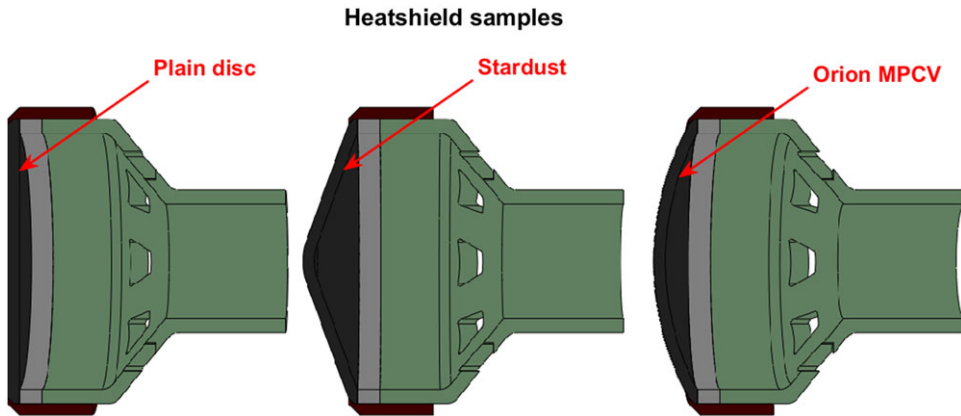
Heatshield samples

Figure 2. *Axisymmetric heatshield samples to be used for re-entry aerothermodynamics studies.*

in Modane (France), EADS, PWK facilities at IRS (Stuttgart), VUT-1 shock tube at MIPT, wind tunnels for space applications at DLR, VKI Plasmatron and mini-torch facilities (Bruxelles), TCM2 that was previously available at IUSTI (Marseille), CORIA (Rouen), IPG-4 Plasmatron at IPM (Moscow) and MESOX at PROMES (Odeillo) [20,21]. For numerical simulations, the difficulty is to interpret the chemical reaction processes correctly because of the fact that flight test data have demonstrated discrepancies from both numerical simulations and wind-tunnel experiments [19]. In the present work, these high-enthalpy problems are completely eliminated and the surface temperature is completely responsible for the actual dissociation and recombination of re-entry gases. The rationale behind this innovation is to achieve an alternative thermal coupling of gas–surface interactions with a high degree of confidence. The credibility demonstrated for extreme re-entry problems makes the present work an indispensable tool for re-entry aerothermodynamics studies. As shown in Fig. 2, the heatshields of the studied vehicles are generally axisymmetric and generate heat at re-entry as a consequence of the drag that is used to reduce their speed [22]. Flow parameters such as enthalpy, stagnation pressure, velocity and heat flux also continue to change rapidly during re-entry [23]. The novel plasma preheating methodology presented herein can be used to investigate the aerothermodynamics during the re-entry of all axisymmetric blunt bodies. Three heatshield samples are considered in the present work. Each with a diameter of 50 mm and a uniform thickness of 2 mm was mounted on a probe (very similar to the European standard probe) and heated from the downstream side using a plasma to temperatures in excess of 3000K.

2.0 OVERVIEW

Reliable heat-shielding is essential, physical re-entry processes are complicated, experiments are needed to support model development and hypersonic impulse facilities cannot perform ablation tasks if cold-walled. The aim of the current work is to achieve high thermal and aerodynamic performance at lower cost. The Next-Generation Experimental Model (NGEM) presented in this work is very similar to the European standard probe but comes with six degrees of freedom to account for the variable angle-of-attack for better manoeuvrability during re-entry, descent and landing. This increased operational capability represents a milestone achieved by the NGEM. Recent experiments based on Orion re-entry conditions used a surface temperature of about 2800K [24] and the Apollo 4 lunar return speed of 11 km/s reportedly resulted in a surface temperature of about 2400K [25], while typical re-entry surface temperatures for Space Shuttles were about 1740K [24]. The author had previously used the new plasma preheating test device to achieve a surface temperature of about 2500K on a preheated graphite surface
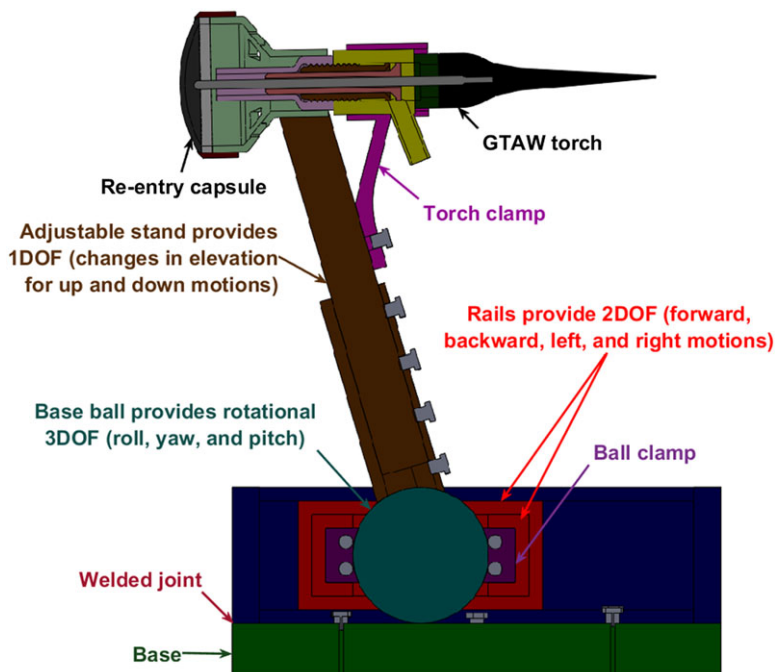
Figure 3. *Sectional view showing improved operational capabilities for the NGEM (see Appendixes for details).*

[26]; the surface temperature profile was then used to assess the mass loss through ablation in a Mach 4.5 flow [27]. The use of this invention as a means of heating the disk has been proven to be effective for reaching temperatures of this magnitude [28], and the process has potential to be used more widely for ablation experiments [29]. This innovative research work makes a significant contribution to hot-wall testing of carbon-based materials for ablation and re-entry studies in hypersonic impulse facilities.

The aim of the present work is to improve the setup for generating the plasma to enable the components to tolerate higher temperatures and improve the aerothermodynamic capability of future experimental programs. The advantages associated with the new plasma preheating technique include (1) the light weight and portability of the model, (2) the control over the surface temperature to replicate re-entry conditions, (3) the excellent temperature profile across the surface of the sample, (4) the ability to replicate entries for different planetary missions due to its capability to perform well in all types of re-entry gases such as O_2, N_2, Air, CO_2, He, Ne, Ar, H_2, CH_4, NH_3, etc.; (5) the ability to be applied to different types of heatshield materials such as PICA, SIRCA, Avecoats, C/C composites, graphite, etc.; (6) the ability to be used for different axisymmetric probe geometries such as Stardust, Orion, Hayabusa, SpaceX-dragon, etc.; (7) the ability to perform well in both short- and long-duration wind tunnels; and (8) its highly economical nature, as the operational costs are less than 10% of those of running the high-enthalpy plasmatron and NASA Ames arc-jet facilities. In addition to the above-mentioned advantages, this present work optimised the aerothermodynamic efficiency for future experimental tests and can now generate stagnation point temperatures above 3000K. The two major improvements associated with the NGEM are: (a) a reduction of the heat losses via conduction on the heatshield sample by incorporating a thermal barrier between the test sample and the backshell, and (b) the incorporation of six degrees of freedom to account for variable angle of attacks for better manoeuvrability during re-entry, descent and landing. These modifications enable the NGEM to be smarter and more practically replicate real flight vehicles, as shown in Fig. 3.
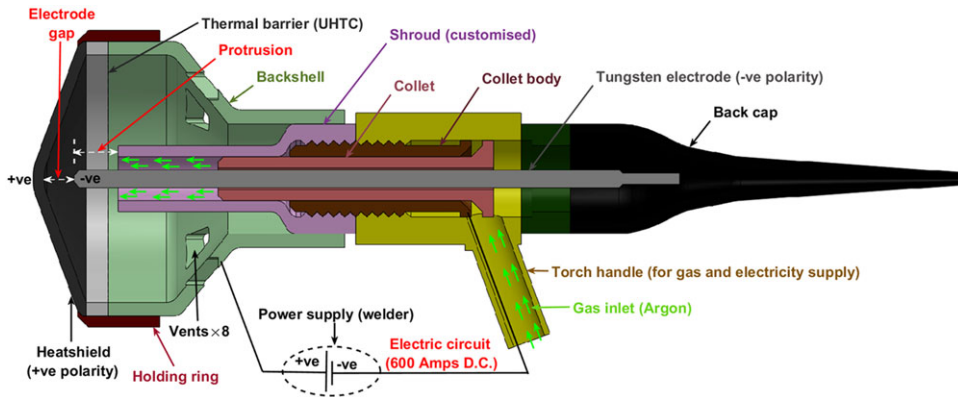
Figure 4. *Schematic layout of setup for ablation experiments.*

3.0 METHODOLOGY

The technique uses a plasma preheating source with an argon flow, and the model in the present work can be likened to an improved version of the European Standard Probe [30,31] but with six degrees of freedom (6DOF) to account for variable angle of attacks during planetary entries. The separation of the tungsten electrode from the disk surface and the length that the electrode protrudes from the shroud affect the ability to start a plasma [32]. Preheating of the heatshield was achieved using a plasma [33,34] generated by a Direct-Current (DC) [35,36], occupying the electrode gap as shown in Fig. 4.

The two most important geometric parameters controlling the heat flux to the workpiece (heatshield) are the electrode gap and protrusion. The orientation of the Tungsten Inert Gas (TIG) electrode is centralised in the model to enable even thermal spread from the centre to the edges and enable the probe model to assume an axisymmetric orientation. As the inert gas (argon) flows over the tungsten electrode and approaches the heatshield, the enthalpy increases drastically as a result of radiative heating by the hot plasma. On reaching the heatshield, the argon gas almost reaches an equilibrium temperature with the hot plasma. Figure 5 shows a cross-sectional view of the model that illustrates the heat transfer processes from the hot plasma to the heatshield. The ceramic shroud and thermal insulator will be made of Z105 zirconia (ZrO_2). Zirconia is an extremely refractory material with low electrical and thermal conductivities [37] and a melting point of about 3100K [38]. The holding ring can be made of any metallic conductor, but for the purpose of thermal survivability, the holding ring will be made of titanium carbide Ultra-High-Temperature Ceramics (UHTC). Titanium carbide has high electrical conductivity, high chemical stability and a high melting point of about 3140°C [39] but a low thermal conductivity of about 5.64W/m-K at 1000°C [40]. The backshell will be made of stainless steel, and the normal Gas Tungsten Arc Welding (GTAW) accessories will be purchased.

Graphite was selected as a representative heatshield material in Fig. 5 because of its associated advantages. Carbon is the basic ingredient for the majority of ablative heatshield materials [41]. Graphite is considered to be the basic carbon material for assessing ablation properties [42,43]. Graphite remains a class of superior carbonaceous material because it possesses refractory ability, high thermal shock resistance, good mechanical strength at high temperatures, excellent machinability, high thermal conductivity, high sublimation temperature, relatively low oxidation rate and low material cost [44]. The graphite used in the present work is an iso-statically pressed graphite with grade PCC-X2 from Graphite Australia with the properties listed in Table 1. Analysis of other materials can be made by simply reproducing the methodology and replacing the properties of the disc material in the simulations.

Some of the significant improvements in the NGEM for the purpose of improving the thermal capability of the invention in order to reliably replicate planetary re-entry surface temperatures with a high degree of confidence are presented in Table 2.
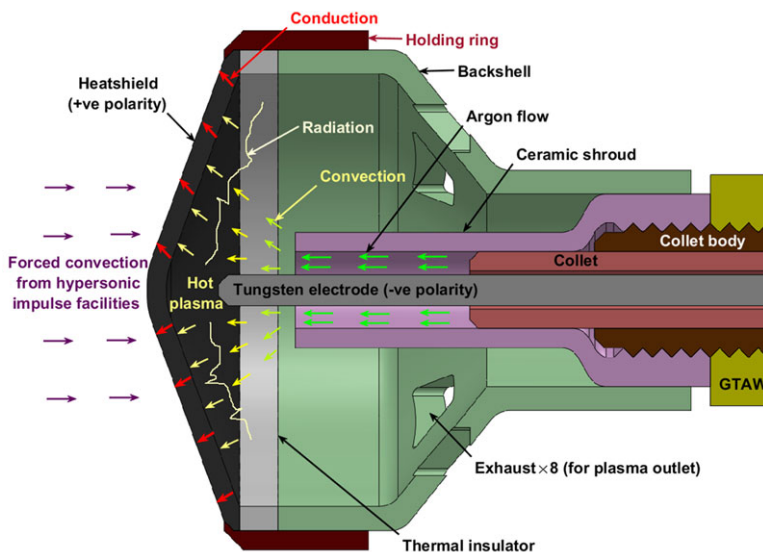
Figure 5. *Illustration of heat transfer processes from hot plasma to the heatshield.*

Table 1. *Physical properties of PCC-X2 graphite, where CTE refers to the coefficient of thermal expansion*

Bulk density	Maximum particle size	Rockwell hardness	Compressive strength	Flexural strength
1.78 g/cm ^{3}	0.045 mm	85	60 MPa	30 MPa

Other properties of PCC-X2 graphite				
Porosity	**Specific resistance**	**Ash content**	**Thermal conductivity**	**CTE**
12–14%	8.0μΩm	0.05%	95W/(m.K)	$2.7 \times 10^{-6} K^{-1}$

Table 2. *Materials selection for components and parts in the NGEM to be used for ablation experiments*

| Part	Material/features	Scientific relevance
Backshell thickness	2.5mm	Reduced mass and heat-sink effects
Geometry	Advanced	Better thermodynamic performance
Thermal barrier system	Present	Reduced conduction losses
Holding ring	TiC	Higher thermal capability over steel
Backshell	Mild steel	Housing and support
Ceramic shroud	Zirconia	Higher thermal capability over 96% alumina
GTAW torch	Attached	Thermal optimisation over detached features
Stand	Adjustable	Flexibility in elevations
6DOF	Present	Better aerodynamic manoeuvrability
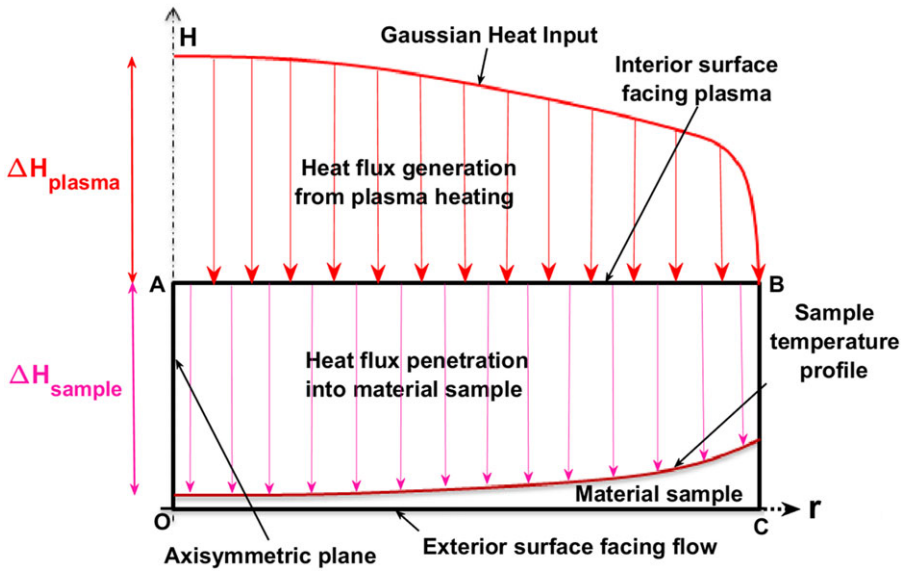
Figure 6. *Schematic heat flux domain with boundary conditions in the plasma preheating test device.*

4.0 ESTIMATING POWER REQUIREMENTS

The heat flux has a direct correlation with the surface temperature, which follows a Gaussian distribution from the stagnation point to the edges [45]. As shown in Fig. 6, the method consists of splitting a heatshield sample along the axisymmetric plane (OA) and measuring the heat flux to one of the edges as a function of radius (*r*) relative to the splitting plane. The radial heat distribution can then be derived using Abel transformation of the heat flux measurements [46].

4.1. Boundary conditions

(1) As shown in Fig. 6, the material sample is block OABC, representing a half portion of a circular disk;

(2) Line AB represents the surface facing the plasma, while OC is the surface facing the flow;

(3) Line OA represents the axisymmetric plane;

(4) The heat flux generation from plasma heating follows a Gaussian distribution;

(5) The heat flux penetration into the material sample has a direct correlation with the plasma temperature;

(6) The material surface (AB) facing the plasma can be either perpendicular to the plasma (for disk samples) or concave to the plasma (for Orion and Stardust samples).

(7) The surface temperatures attain steady-state conditions just before the flow starts.

4.2. Governing heat equation

An analytical method was used to estimate the power requirements for preheating the samples. For this analysis, electrical power is the dominant source of energy input. The governing heat equation for the heatshield material sample is given by Equation (1).

$$Rate\ of\ energy\ input = thermal\ energy\ transfer + thermal\ energy\ storage \tag{1}$$

$$\therefore\ Electrical\ power = thermal\ [conduction + convection + radiation] + energy\ storage \tag{2}$$

$$I^2R = \overbrace{\frac{\delta}{\delta r}k\frac{dT}{dr}}^{\text{Conduction}} + \overbrace{Ah\,(T - T_\infty)}^{\text{Convection}} + \overbrace{A\varepsilon\sigma\,(T^4 - T_\infty^4)}^{\text{Radiation}} + \overbrace{\rho c_p\frac{dT}{dt}}^{\text{Storage}} \tag{3}$$

where I represents the current rating, R is the resistance of specimen, k is the thermal conductivity of the material, $\frac{dT}{dr}$ is the temperature gradient in the radial direction, A is the area of heat application, h is the convective heat transfer coefficient, T is the surface temperature, T_∞ is the ambient temperature, ρ is the density of the material sample and c_p is the specific heat capacity of the material sample. Conductive heat transfer from the disk to the backshell can be neglected due to thermal barrier/insulation. The convective heat transfer can also be neglected due to the vacuum conditions as the convective heat transfer coefficient approaches zero prior to flow. Also prior to flow, the heatshield material is thermally soaked and a steady-state condition is achieved as $\frac{dT}{dt}$ approaches zero. Hence, Equation (3) reduces to Equation (4). This approximation is reasonable because, at temperatures in excess of 2000K, the conductive and radiative heat transfers become increasingly negligible compared with radiative heat transfer.

$$I^2R = \overbrace{A\varepsilon\sigma\,(T^4 - T_\infty^4)}^{\text{Radiation}} \tag{4}$$

Considering a disk of arbitrary radius dr and uniform cross-sectional area A_{cs} with resistivity μ, the electrical resistance is given by Equation (5):

$$R = \mu\frac{dr}{A_{cs}} = \mu\frac{dr}{\pi r^2} \tag{5}$$

The surface temperature of the sample can then be estimated based on radiative heating from the plasma. Equating the total electrical power to the radiative heating, where the source of heat flux for the heatshield is the plasma inside the probe, yields Equation (6), where I is the current, R is the resistance of material sample, ε is the emissivity of the sample material, A is the total surface area of sample being exposed, σ is the Stefan–Boltzmann constant and T is the surface temperature.

$$I^2R = A\varepsilon\sigma\,(T^4 - T_\infty^4) \tag{6}$$

Taking A to be $2\pi r^2$ for the front and back side of the disk and substituting the value for R in Equations (5) into (6), it can be shown that the temperature T is given by Equation (7):

$$T = \left[I^2\mu\frac{dr}{2\pi^2\varepsilon\sigma r^4} + T_\infty^4\right]^{0.25} \tag{7}$$

Similarly, the temperature variation with radius of the Orion sample can be calculated by substituting $\pi\,(d^2r + h^2)$ for the front surface area, where h is the maximum height of the spherical cap perpendicular to the base. Also, the surface area of the stardust geometry can be obtained from literature. This simple One-Dimensional (1-D) analysis appeared to be reasonable for estimation purposes because it showed good correlation to calibrated data. Figure 7 shows the surface temperatures estimated using Equation (7), and by substituting 28×10^{-4}Ohm.m for electrical resistivity, 0.9 for emissivity *and* 5.68^{-8}W/m^{4}K for the Stefan–Boltzmann constant, the non-linear relation between the current rating and surface temperature is shown in Fig. 7, which is the average power requirement for all three sample. The heating started from ambient temperature (T_∞) and shows good agreement with calibrated data. Temperature calibration was carried out using currents of 200A, 250A, 300A, 350A and 400A. The calibration was limited to a maximum current of 400A during preliminary tests because of the limitations in the material thermal capabilities [28]. With the present material selection as presented in Table 2 for the experimental model, a current of 600A can be practically applied to achieve stagnation point temperatures in excess of 3000K.

The present work adopts heatshields of constant thickness of 2 mm, considered suitable for ablation experiments. Using graphite material and a current rating of 400A, it took about 15s for the plain disk
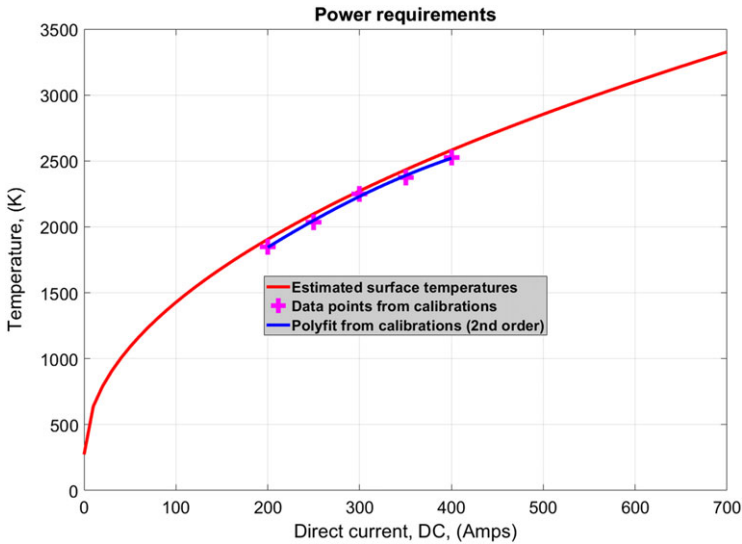
Figure 7. *Average power requirements for preheating surface temperatures.*
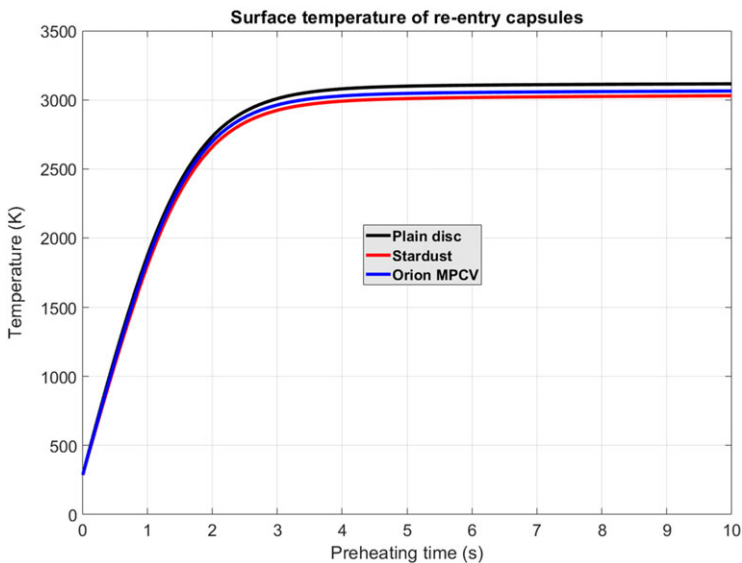

Figure 8. *Transient simulation of stagnation surface temperatures with heatshields of 2mm thickness.*

sample to attain steady state. The present work is designed for a current rating of 600A. Using this current and invoking the graphite material properties from Table 1 in a Finite-Element Analysis (FEA) simulation using Ansys, it took about 8s for the samples to attain steady-state temperatures, as shown in Fig. 8. The apparatus development for the new preheating methodology, the camera and spectrometer calibration, and the FEA simulations show that the determined temperature profile of the heated disc is suitable to continue with mass loss assessments [28]. This work focuses on ground-based characterisation techniques for thermal protection material analysis, thus making it a valuable tool for to study aerothermodynamics during re-entry. The presented technology is useful for detailed material characterisation, for example, in the context of material response model validation.

4.3. Abel's transformation for heat flux distributions

Suppose that (y_1, y_2) are linearly independent solutions of a homogeneous second-order differential equation given by Equation (8) on (a, b), where $A(x)$, $B(x)$ are continuous on (a, b), then the round scheme $W(x)$ is either always zero on (a, b) or never zero on (a, b). For $x \in (a, b)$, this can be mathematically analysed as follows:

$$y'' + A(x)\, y' + B(x)\, y = 0 \tag{8}$$

$$\text{Set } W = W(y_1, y_2) = \begin{vmatrix} y_1 & y_2 \\ y_1' & y_2' \end{vmatrix} = y_1 y_2' - y_2 y_1' \tag{9}$$

Differentiating Equation (9) using the product rule produces Equation (10)

$$\therefore W' = \left[y_1 y_2'' + y_2' y_1' \right] - \left[y_2 y_1'' + y_1' y_2' \right] = y_1 y_2'' - y_2 y_1'' \tag{10}$$

Since (y_1, y_2) are solutions, they can independently fit into Equation (8), resulting in

$$y_1'' + A(x)\, y_1' + B(x)\, y_1 = 0 \tag{11}$$

$$\rightarrow y_1'' = -A(x)\, y_1' - B(x)\, y_1 \tag{12}$$

Also,

$$y_2'' = -A(x)\, y_2' - B(x)\, y_2 \tag{13}$$

Substituting the expressions for y_1'' and y_2'' in Equation (12) and Equation (13) into the Right-Hand Side (RHS) of Equation (10) gives

$$W' = y_1 \left[-A(x)\, y_2' - B(x)\, y_2 \right] - y_2 \left[-A(x)\, y_1' - B(x)\, y_1 \right] = A(x)\, y_2 y_1' - A(x)\, y_1 y_2' \tag{14}$$

$$\therefore W' = A(x)\, y_2 y_1' - A(x)\, y_1 y_2' = A(x)\, (y_2 y_1' - y_1 y_2') = A(x)\, (-W) \tag{15}$$

$$\rightarrow \frac{dW}{dx} = -A(x)\, (W) \rightarrow \frac{dW}{W} = -A(x)\, dx \tag{16}$$

Integrating both sides of Equation (16) will produce Equation (17), where C is the constant of integration:

$$\ln W = -\int_{x_0}^{x} A(x)\, dx + C \tag{17}$$

Taking the exponential of both sides of Equation (17) yields

$$W = exp^{-\int_{x_0}^{x} A(x)dx} + exp^{C} = exp^{-C\int_{x_0}^{x} A(x)dx} = C exp^{-\int_{x_0}^{x} A(x)dx}$$

Hence,

$$W(r) = W(r_0)\, exp^{-\int_{r_0}^{r} A(r)dr} \tag{18}$$

Equation (18) shows the initial boundary conditions, where the constant C represents $W(r_0)$. If C is zero, then the whole expression for $W(r)$ will be zero. Alternatively, if C is not zero, then the whole expression for $W(r)$ can never be zero because the value of an exponential function does not reach zero. The distribution of the net heat flux reaching the heatshield is taken to be a Gaussian distribution, where the net flux falls onto an area of heat application of a given radius (AB), as shown in Fig. 6. The spatial variation of the net flux, $q(r)$, falling onto a workpiece from the arc source as a function of the (heat) flux distribution parameter in the radial direction, r, had similarly been reported by Goldak et al. [47], as presented by Arul and Sellamuthu [48], where Q_{max} is the maximum heat intensity for a stationary heat source.

$$q_r = Q_{max}\, exp^{-\left[\frac{6r^2}{AB^2}\right]} \tag{19}$$

The arc efficiency is expressed as $\mu = \frac{Q_{Net}}{I \times V}$, where Q_{Net} is the net heat flux, I is the current and V is the applied voltage. The arc length is the primary parameter governing the heat distributions, while the current dominates the magnitude of the heat flux on the anode surface [46].
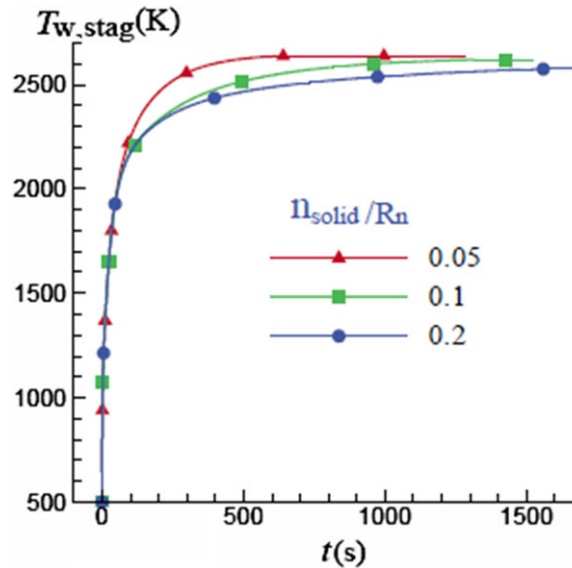
Figure 9. *Ablation of graphite in dissociating air with different thicknesses [49].*

5.0 PREHEATING TIME VERSUS THICKNESS OF HEATSHIELD SAMPLES

Simulations from other work have shown that the time required to reach steady state became longer as the heatshield thickness increased, as shown in Fig. 9. The time evolution of the heatshield thickness along the stagnation line was investigated through numerical simulations, where n_{solid} is the heatshield thickness (0.05, 0.1 and 0.2m), Rn is a constant nose radius of 1m, and t is the heating time in seconds. Using constant heating, the 0.05m sample (red line) attained a steady-state condition at about 450s, the 0.1m sample (green line) attained steady state at about 1100s and finally the 0.2m sample (blue line) attained its steady state at about 1500s.

The decision about the thickness should be properly considered to balance the preheating costs and the aerodynamic loads. Although thinner samples save time and operational costs, the aerodynamic loading on a sample supported around the edges with a very small thickness will likely be too high, and the sample will break, thereby rendering the experiments useless. The thermal expansion loads needed to maintain electrical conductivity between the heatshield and electrode, unavoidable aerodynamic forces and other constraints resulting from holding the samples will exacerbate any potential for failure of the specimens.

6.0 SIMULATION RESULTS FROM PLASMA PREHEATING

The temperature contours displayed in Fig. 10 show that the thermal distribution was highly axisymmetric with minimal edge effects. The temperature distributions of the experimental probes were simulated using Three-Dimensional (3D) FEA with Ansys. The simulation was for no-flow, and the heat flux inputs were tuned to produce the surface temperatures at 600A current rating. For the computational setup, the grid resolution was smooth and the meshing adaptive. The boundary conditions were mainly applied to the heatshield samples, and the heat gradually flowed towards the surrounding materials. The simulation results correspond to a heating duration of 10s. Although steady-state conditions were attained at about 8s, the additional preheating time provided room for any noticeable thermal soak after the solution reached steady state. As the solutions run beyond 8s, additional thermal soak was not really an issue in the present work (Fig. 8). The surface temperatures of the samples exceeded 3000K at the stagnation point, decreasing non-linearly from the stagnation point to about 2600K at the edges, as shown in Fig. 11.
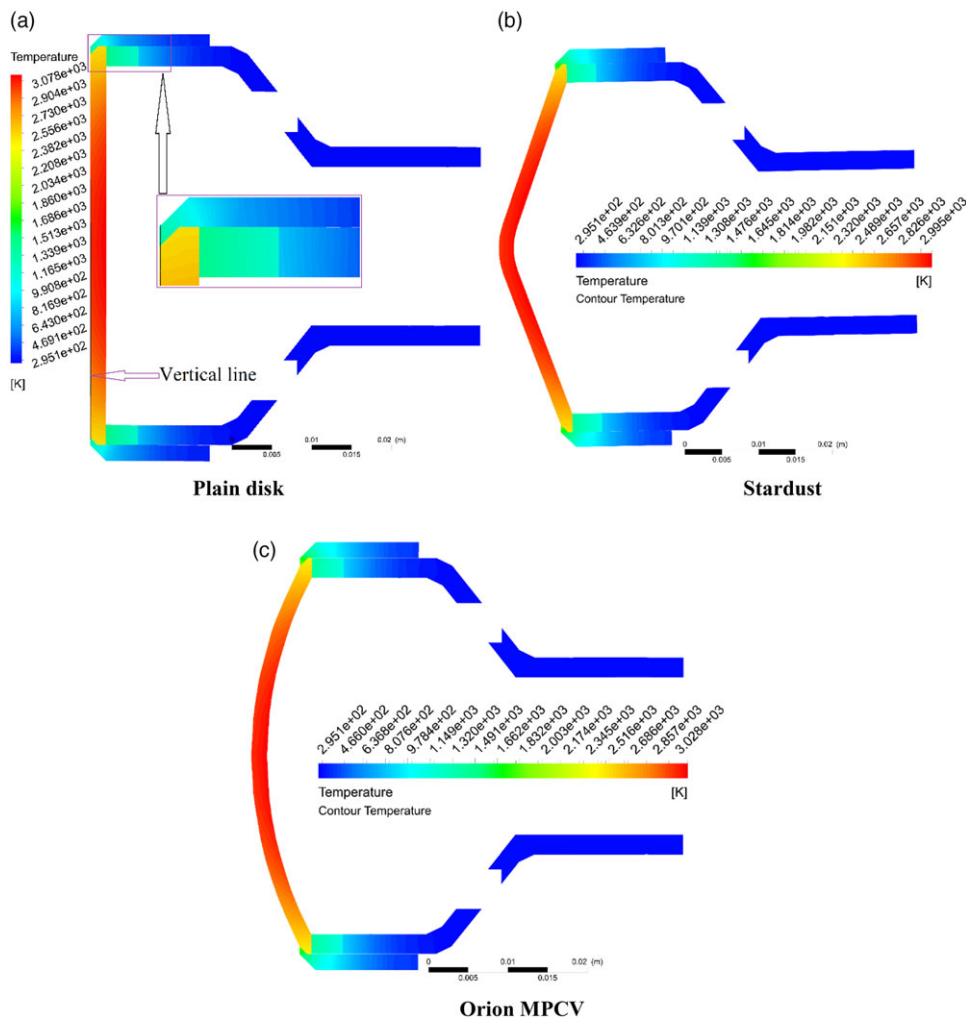
Figure 10. *Temperature contours of selected heatshield samples from FEA simulations showing heatshield thermal spread for the NGEM at no-flow conditions.*

Figure 10 shows the temperature contour from the FEA simulation using Ansys Workbench. The contact regions in the present work have been designed to minimise conduction losses at the heatshield edges (shoulder regions) using a thermal barrier material (zirconia). The improvement of the surface temperature profile in the present work can be seen in Fig. 11. For the present work, Fig. 11 shows the surface temperature profile of a graphite heatshield at the stagnation point in excess of 3000K, gradually decreasing to about 2550K at the shoulder regions (points A and B). Beyond the shoulder regions a holding ring is in contact with the heatshield (points E and F), where the temperature first experiences a drastic drop (to about 1500K) due to the low conductivity across the contact and the high thermal diffusivity of metallic material, and further experiences a thermal drop to about 1300K on surfaces in contact with the environment (points G and H). Details regarding the spatial temperature profiles have been exhaustively published by the author [28,29].

7.0 SPATIAL TEMPERATURE DISTRIBUTION

Axisymmetric heatshield samples must have a good temperature distribution for accurate aerothermodynamics quantification of ablation rates in hypersonic impulse facilities. One of the fascinating advantages
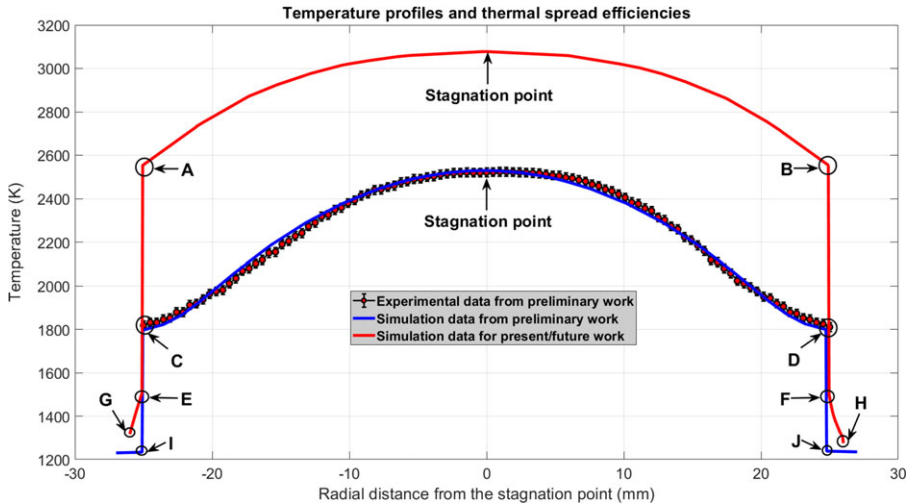
Figure 11. *Spatial temperature profiles showing heatshield thermal spread [28].*

of this new plasma preheating technique is the surface temperature control of the ablation sample in a hypersonic flow field. The surface temperatures can be regulated to replicate re-entry requirements in hypersonic impulse facilities. Due to the strong coupling between surface temperatures and boundary-layer species, the surface temperature profile needs to be well established to be able to reflect the boundary-layer characteristics. Figure 12 shows the temperature contours of a 50mm-diameter axisymmetric heatshield sample predicted using MATLAB Simulink. The thermal spread efficiency is a very important aspect of surface temperature control. The top left of Fig. 12 shows a very poor temperature distribution from the stagnation point to the edges. At the top right, the spatial temperature distributions of the axisymmetric heatshield sample are improved but still show a poor profile from the stagnation point to the edges. The temperature profile is further improved at the bottom left, and finally, the bottom right image shows a very good temperature profile across the disk because of the good thermal spread efficiency from the stagnation point to the edges. It is interesting to note that all four images in Fig. 12 have the same temperature of about 3100K at the stagnation point. Obtaining a good stagnation point temperature without reference to the overall surface temperature profile will be completely unreliable for any re-entry aerothermodynamics studies. A good surface temperature coupled with aerodynamic pressure, oxidiser composition, flow strain rate (as functions of model shape and amount of burn-off) and material properties always results in a good boundary-layer characteristic due to the strong coupling between the gaseous and surface kinetics.

8.0 PHYSICAL EXPLANATIONS

The CFD results using an axisymmetric graphite sample showed a good temperature distribution for ablation rate experiments in hypersonic impulse facilities. Figure 13 illustrates the flow dynamics and associated aerothermodynamic gradient along the surface, where the source of heat flux for the heatshield is the plasma inside the probe. The temperature is driven by the plasma at the back side of the experimental sample, while the aerodynamic flow is driven by the forced convection from the hypersonic impulse facility at the front side of sample (heatshield specimen). The aerodynamic flow velocity at the surface of the experimental sample increases from the stagnation point to the edges, while the surface temperature decreases from the stagnation point to the edges.

While the aerothermodynamic flow (cooling of sample) occurs at the front, the plasmadynamic flow (heating of sample) occurs at the back side of the disk. The plasma zone is a term used to describe the region occupied by the plasma. At steady-state condition, the inert gas flows through the shroud,
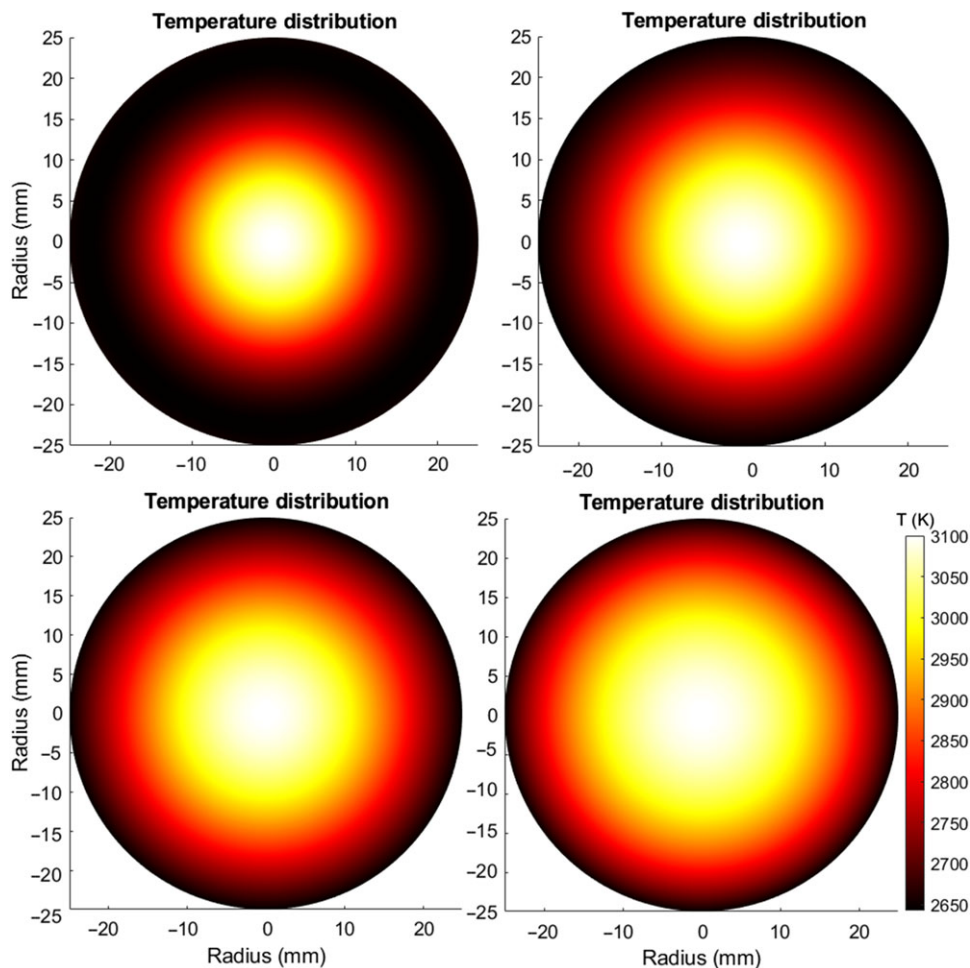
Figure 12. *Temperature distributions of axisymmetric heatshields (viewing normal to the surface).*

gains some heat energy from the centralised hot tungsten electrode, then experiences a drastic rise in enthalpy as it passes through the hot plasma towards the heatshield, before finally exiting via the exhaust/vent.

Some preliminary experiments were carried out to validate this novel plasma preheating test device. A 50mm disk sample was heated with plasma in a vacuum of 500Pa, then the hot sample was subjected to Mach 4.5 flow for 0.5s, as shown in Fig. 14(a). The Schlieren technique based on the principle of the changing density of the gas was used to identify the establishment of the bow shock and therefore the commencement of Mach 4.5 flow. The high-speed camera was set at a frame rate of 2500fps. Detailed numerical analyses have been provided extensively by the author in other publications [26–29], where the ablation rate gradually decreased from the stagnation point to the edges of the disk. CO formation was the major contributor to graphite mass loss, while the contributions from all other carbonaceous species were relatively insignificant. All carbonaceous species shoed peak values around the stagnation region at the wall. The sample data from simulations using Stardust and Orion MPCV show general agreements with that of the disk. Due to the good thermal coupling between the surface and the flow, the present work has potential to be a better analytical/experimental research tool for simulating reaction species for different planetary missions.
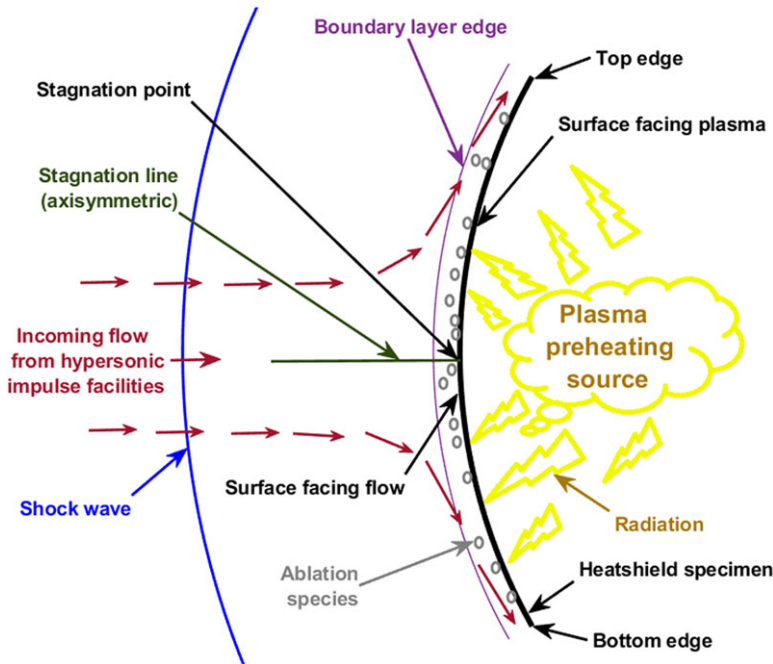
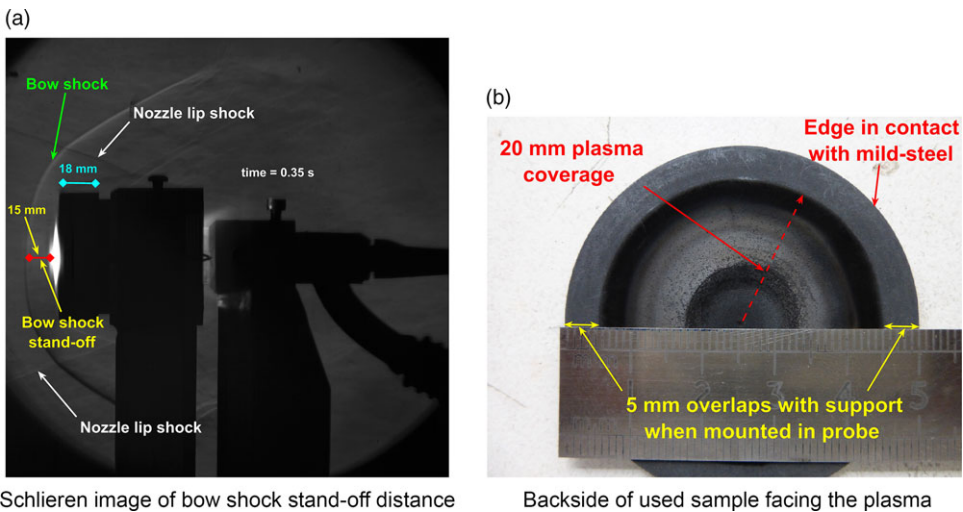**Figure 13.** *Schematic illustration of surface aerothermodynamic flow properties.*

Figure 14. *Preliminary experiments conducted at Mach 4.5 to validate plasma preheating invention [26,28].*

9.0 FUTURE WORK

This novel invention can accurately replicate planetary re-entry surface temperatures and any associated hypersonic flow characteristics within the boundary layer. The NGEM has been fully developed for series of ablation tests in any reliable aerospace laboratory. The fact that the NGEM can replicate surface temperatures in excess of 3000K, will encourage the use of spectroscopic measurements of ablation species and spatial microstructural studies using X-ray microtomography. Infrared pyrometers and thermo-cameras are also needed to adequately monitor the surface temperature profiles across experimental samples.

10.0 CONCLUSIONS

The plasma preheating arrangement described herein represents a novel preheating technique that generates the heat flux needed for the characterisation of surface temperatures without using an arc-jet or plasmatron facility. This technique aims to produce a better method for reliable aerothermodynamic testing to investigate ablation samples of re-entry probes. The probe used is very similar to the European Standard Probe. Also, the plasma technique is very different from the normal resistive heating techniques that are commonly used in expansion/shock tubes. The key to the NGEM is the inclusion of 6DOF to account for the variable angle of attacks for better manoeuvrability during re-entry, descent and landing. This inclusion has never been attempted for re-entry aerothermodynamics studies elsewhere. These modifications will enable next-generation models to be smarter and more practically replicate real flight vehicles. This intellectual property is not classified elsewhere and will significantly aid all re-entry aerothermodynamics studies while also making an extremely useful contribution to improving the reliability of aeroheating testing in hypersonic impulsive facilities around the world.

References

[1] Schneider, S.P. Laminar-turbulent transition on reentry capsules and planetary probes. *J. Spacecraft Rockets*, 2006, **43**, (6), pp 1153–1173.

[2] Liechty, D., Hollis, B. and Edquist, K. Control Surface and Afterbody Experimental Aeroheating for a Proposed Mars Smart Lander Aeroshell. In *AIAA Atmospheric Flight Mechanics Conference and Exhibit* (p. 4506), 2002.

[3] Edquist, K.T., Liechty, D.S., Hollis, B.R., Alter, S.J. and Loomis, M.P. Aeroheating environments for a Mars smart lander. *J. Spacecraft Rockets*, 2006, **43**, (2), pp 330–339.

[4] Wang, Z.H., Yu, Y.L. and Bao, L. Heat transfer in nonequilibrium flows with homogeneous and heterogeneous recombination reactions. *AIAA J.*, 2018, **56**, (9), pp 3593–3599.

[5] Gülhan, A., Esser, B., Koch, U., Fischer, M., Magens, E. and Hannemann, V. Characterization of high-enthalpy-flow environment for ablation material tests using advanced diagnostics. *AIAA J.*, 2018, **56**, (3), pp 1072–1084.

[6] Riccio, A., Raimondo, F., Sellitto, A., Carandente, V., Scigliano, R. and Tescione, D. Optimum design of ablative thermal protection systems for atmospheric entry vehicles. *Appl. Therm. Eng.*, 2017, **119**, pp 541–552.

[7] Gnoffo, P.A. Planetary-entry gas dynamics. *Annu. Rev. Fluid Mech.*, 1999, **31**, (1), pp 459–494.

[8] Collicott, H.E. and Bauer, P.E. *Entry Vehicle Heating and Thermal Protection Systems: Space Shuttle, Solar Starprobe, Jupiter Galileo Probe*, American Institute of Aeronautics and Astronautics, 1983.

[9] Wang, Z.H., Yu, Y.L. and Bao, L. Heat transfer in nonequilibrium flows with homogeneous and heterogeneous recombination reactions. *AIAA J.*, 2018, **56**, (9), pp 3593–3599.

[10] Gülhan, A., Esser, B., Koch, U., Fischer, M., Magens, E. and Hannemann, V. Characterization of high-enthalpy-flow environment for ablation material tests using advanced diagnostics. *AIAA J.*, 2018, **56**, (3), pp 1072–1084.

[11] Mortensen, C.H. and Zhong, X. Real-gas and surface-ablation effects on hypersonic boundary-layer instability over a blunt cone. *AIAA J.*, 2016, **54**, (3), pp 980–998.

[12] Poovathingal, S., Schwartzentruber, T.E., Murray, V.J. and Minton, T.K. Molecular simulation of carbon ablation using beam experiments and resolved microstructure. *AIAA J.*, 2016, **54**, (3), pp 999–1010.

[13] Lei, L., Guangyue, D., Lei, Z., Zhenfeng, W. and Yewei, G. Experimental model design and preliminary numerical verification of fluid–thermal–structural coupling problem. *AIAA J.*, 2019, **57**, (4), pp 1715–1724.

[14] Sagnier, P. and Verant, J.L. Flow characterization in the ONERA F4 high-enthalpy wind tunnel. *AIAA J.*, 1998, **36**, (4), pp 522–531.

[15] Horvath, T.J., Berry, S.A. and Merski, N.R. *Hypersonic boundary/shear layer transition for blunt to slender configurations-A NASA Langley experimental perspective*, National Aeronautics and Space Administration Hampton Va Langley Research Centre, 2004.

[16] Sheikh, U.A., Morgan, R.G. and McIntyre, T.J. Vacuum ultraviolet spectral measurements for superorbital earth entry in X2 expansion tube. *AIAA J.*, 2015, **53**, (12), pp 3589–3602.

[17] Davies, C. and Arcadi, M., 2006. Planetary mission entry vehicles quick reference guide. Version 3.0.

[18] Hollis, B.R. and Borrelli, S. Aerothermodynamics of blunt body entry vehicles. *Prog. Aerosp. Sci.*, 2012, **48**, pp 42–56.

[19] Jiang, Z., Hu, Z., Wang, Y. and Han, G. Advances in critical technologies for hypersonic and high-enthalpy wind tunnel. *Chin. J. Aeronaut.*, 2020, **33**, (12), pp 3027–3038.

[20] Bugel, M., Reynier, P. and Smith, A. Survey of European and major ISC facilities for supporting Mars and sample return mission aerothermodynamics and tests required for thermal protection system and dynamic stability. *Int. J. Aerosp. Eng.*, 2011, **2011**. doi: 10.1155/2011/937629.

[21] Allen, H.J. Some problems of planetary atmosphere entry. *Aeronaut. J.*, 1967, **71**, (684), pp 813–820.

[22] Ostrom, C., Greene, B., Smith, A., Toledo-Burdett, R., Matney, M., Opiela, J., Marichalar, J., Bacon, J. and Sanchez, C., 2019. Operational and Technical Updates to the Object Reentry Survival Analysis Tool.

[23] Asma, C.O., Tirtey, S. and Schloegel, F. Flow topology around gas, liquid and three-dimensional obstacles in hypersonic flow. *AIAA J*, 2012, **50**, (1), pp 100–108.

[24] Glass, D. (2008), Ceramic matrix composite (CMC) thermal protection systems (TPS) and hot structures for hypersonic vehicles, in '15th AIAA International Space Planes and Hypersonic Systems and Technologies Conference', pp 2682-2718.

[25] Dec, J. and Braun, R. (2006), An approximate ablative thermal protection system sizing tool for entry system design, in '44th AIAA Aerospace Sciences Meeting and Exhibit', pp 780-794.

[26] Iyinomen, D.O. Numerical and experimental analyses of ablation measurements in expansion wind tunnel facilities using a new plasma pre-heating technique. *Int. J. Thermofluids*, 2020, **3**, p 100019.

[27] Iyinomen, D.O. Numerical approach to ablation measurements using a new plasma pre-heating technique. *Int. J. Thermofluids*, 2020, **1**, p 100014.

[28] Iyinomen DO, Malpress R and Buttsworth D., Technique development for investigating axisymmetric ablation models in hypersonic impulse facilities. *AIAA J.*, 2021, **59**(6), pp 1899–1913. doi: 10.2514/1.J059629.

[29] Iyinomen, D.O. Technique development for investigation of axisymmetric graphite sample oxidation in hypersonic flow (Doctoral dissertation Institute for Advanced Engineering and Space Sciences, University of Southern Queensland), 2019.

[30] Chazot, O. Experimental studies on hypersonic stagnation point chemical environment, Technical report, Von Karman Institute for Fluid Dynamics Rhode-Saint-Genese (Belgium), 2006.

[31] Loehle, S., Fasoulas, S., Herdrich, G.H., Hermann, T.A., Massuti-Ballester, B., Meindl, A., Pagan, A.S. and Zander, F., 2016. The plasma wind tunnels at the institute of space systems: current status and challenges. In *32nd AIAA Aerodynamic Measurement Technology and Ground Testing Conference* (p. 3201).

[32] Moradi, M., Ghoreishi, M. and Khorram, A., 2018. Process and Outcome Comparison Between Laser, Tungsten Inert Gas (TIG) and Laser-TIG Hybrid Welding. *Lasers in Engineering (Old City Publishing)*, **39**.

[33] Wang, X., Luo, Y. and Fan, D. Investigation of heat transfer and fluid flow in high current GTA welding by a unified model. *Int. J. Therm. Sci.*, 2019, **142**, pp 20–29.

[34] Traidia A. (2011), Multi-physics modelling and numerical simulation of GTA weld pools, PhD thesis, Ecole Polytechnique.

[35] Siewert, E., Baeva, M. and Uhrlandt, D. The electric field and voltage of dc tungsten-inert gas arcs and their role in the bidirectional plasma-electrode interaction. *J. Phys. D Appl. Phys.*, 2019, **52**, (32), p 324006.

[36] Anand, K.R. and Mittal, V. Review on the parametric optimization of tig welding. *Int. Res. J. Eng. Technol. (IRJET)*, 2017, **2017**(4), pp e-ISSN: 2395-0056, p-ISSN: 2395-0072.

[37] Fadda, G., Colombo, L. and Zanzotto, G. First-principles study of the structural and elastic properties of zirconia. *Phys. Rev. B*, 2009, **79**, (21), p 214102.

[38] Ishigame, M. and Sakurai, T. Temperature dependence of the Raman spectra of ZrO2. *J. Am. Ceram. Soc.*, 1977, **60**, (7-8), pp 367–369.

[39] Xiang, M., Song, M., Zhu, Q., Hu, C., Yang, Y., Lv, P., Zhao, H. and Yun, F. Facile synthesis of high-melting point spherical TiC and TiN powders at low temperature. *J. Am. Ceram. Soc.*, 2020, **103**, (2), pp 889–898.

[40] Shackelford, J.F. and Alexander, W. *CRC materials science and engineering handbook*, Boca Raton, FL: CRC press, 2000.

[41] Lachaud, J., Aspa, Y. and Vignoles, G.L. Analytical modelling of the steady state ablation of a 3D C/C composite. *Int J Heat Mass Transfer*, 2008, **51**, (9), pp 2614–2627.

[42] Graves, R. and Gosse, R., Reduced-Order Sensitivity Analysis of an Ablating Graphite Reentry Body. In *51st AIAA Aerospace Sciences Meeting including the New Horizons Forum and Aerospace Exposition* (p. 957).

[43] Lewis, S.W., James, C.M., Ravichandran, R., Morgan, R.G. and McIntyre, T.J. Carbon ablation in hypervelocity air and nitrogen shock layers. *J. Thermophys. Heat Transfer*, 2018, **32**, (2), pp 449–468.

[44] Zeng, M., Liu, J., Xu, D. and Zhang, W.. Numerical study of the transient characteristics of ablative hypersonic flow fields. International Conference on Heat Transfer, Fluid Mechanics and Thermodynamics, 2014.

[45] Bag, S. and De, A. Development of a three-dimensional heat-transfer model for the gas tungsten arc welding process using the finite element method coupled with a genetic algorithm–based identification of uncertain input parameters. *Metall. Mater. Trans. A*, 2008, **39**, (11), pp 2698–2710.

[46] Tsai, N.S. and Eagar, T.W. Distribution of the heat and current fluxes in gas tungsten arcs. *Metall. Trans. B*, 1985, **16**, (4), pp 841–846.

[47] Goldak, J., Chakravarti, A. and Bibby, M. A new finite element model for welding heat sources. *Metall. Trans. B*, 1984, **15**, (2), pp 299–305.

[48] Arul, S. and Sellamuthu, R. Application of a simplified simulation method to the determination of arc efficiency of gas tungsten arc welding (GTAW) and experimental validation. *Int. J. Comput. Mater. Sci. Surf. Eng.*, 2011, **4**, (3), pp 265–280.

[49] Scala, S.M. The Ablation of Graphite in Dissociated Air: *Theory*, Missile and Space Division, General Electric, 1962, pp 1-94.
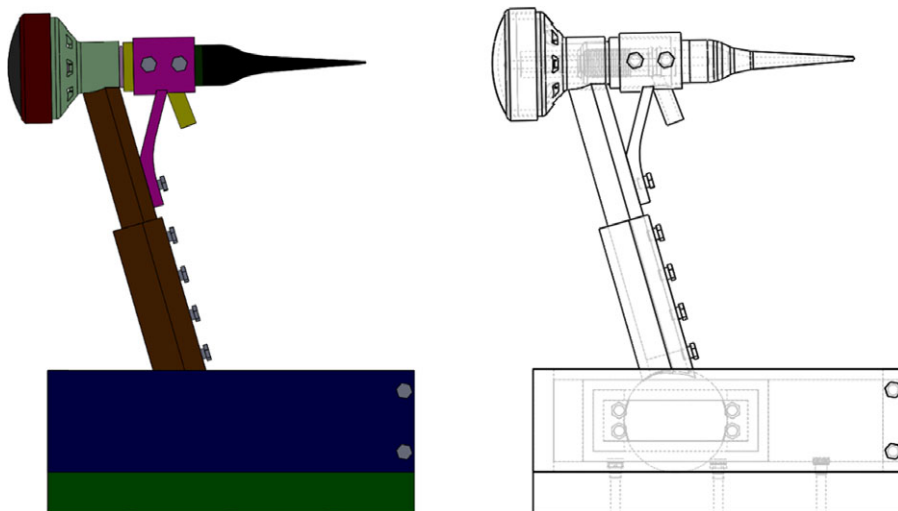
Appendixes

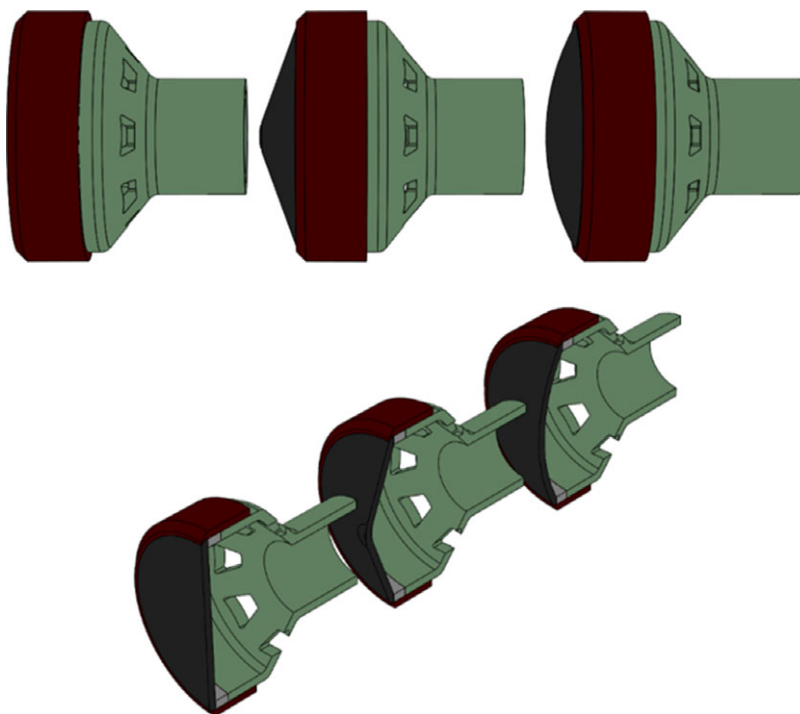***Figure A1.*** *Simplified design of the NGEM (side view)*

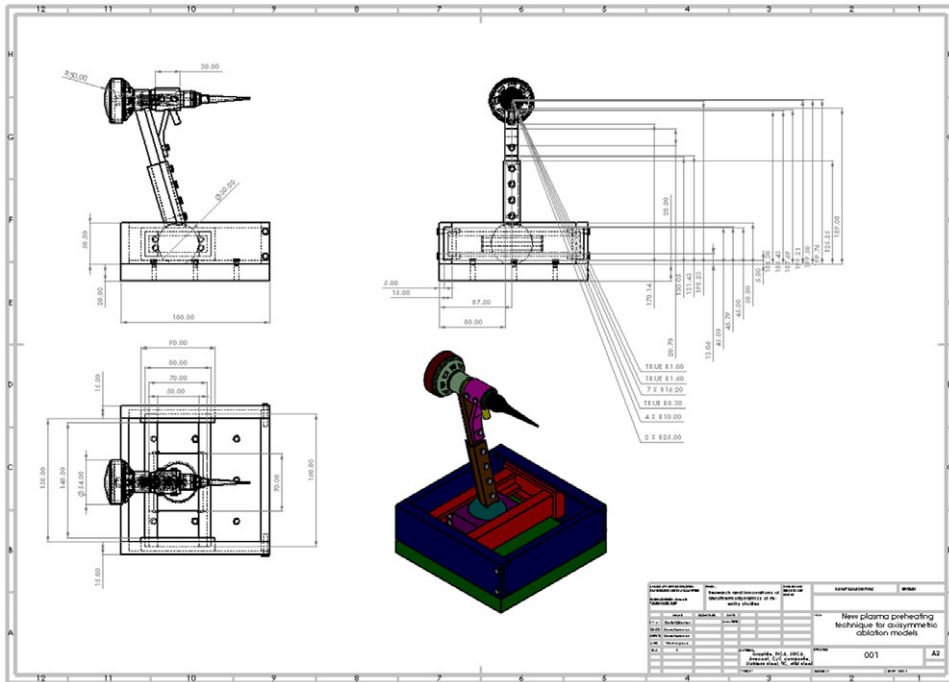***Figure A2.*** *Ablation samples (side view at the top; isometric-sectional view at the bottom).*

Figure A3. *Simplified design of the NGEM (orthographic view).*